A Mechanics-Based Model for 3-D Steering of Programmable Bevel-Tip Needles

Thomas Watts, *Student Member, IEEE*, Riccardo Secoli, and Ferdinando Rodriguez y Baena, *Member, IEEE*

***Abstract*—We present a model for the steering of programmable bevel-tip needles, along with a set of experiments demonstrating the three-dimensional steering performance of a new, clinically viable, 4-segment, preproduction prototype. A multibeam approach based on Euler–Bernoulli beam theory is used to model the novel multisegment design of these needles. Finite element (FE) simulations for known loads are used to validate the multibeam deflection model. A clinically sized (2.5 mm outer diameter), 4-segment programmable bevel-tip needle, manufactured by extrusion of a medical-grade polymer, is used to conduct an extensive set of experimental trials to evaluate the steering model. For the first time, we demonstrate the ability of the 4-segment needle design to steer in any direction with a maximum achievable curvature of $(0.0192 \pm 0.0014\ \mathrm{mm}^{-1})$. FE simulations confirm that the multibeam approach produces a good model fit for tip deflections, with a root-mean-square deviation (RMSD) in modeled tip deflection of 0.2636 mm. We perform a parameter optimization to produce a best-fit steering model for experimental trials with a RMSD in curvature prediction of $1.12 \times 10^{-3}\,\mathrm{mm}^{-1}$.**

***Index Terms*—Medical robotics, robot kinematics, soft robotics.**

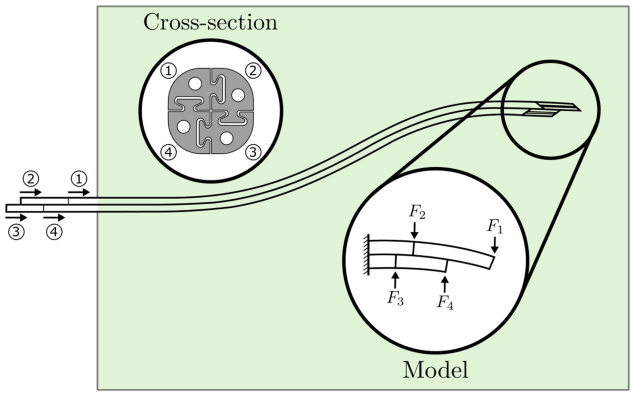

Fig. 1. Diagram showing insertion of a 4-segment programmable bevel-tip steerable needle into soft tissue. The shape of the tip is controlled by the relative insertion of the 4 segments, which determines how the needle steers through the tissue. We propose a multibeam model of the needle tip, as shown, to predict the steering of programmable bevel-tip needles. The design of the cross-section is shown, including an interlocking mechanism to hold the comprising segments together, and a lumen per segment for clinical applications.

I. Introduction

THE last few decades have seen an increase in popularity of minimally invasive procedures, with a growing number of conventional open surgical procedures now being performed by means of rigid tool insertion, either through small ports in the skin (e.g., laparoscopy) or a keyhole aperture in the skull (e.g., keyhole neurosurgery). This shift in surgical approach has been brought about by technical advances in minimally invasive techniques, achieving reduced patient trauma, shorter recovery time, lower chance of infection, and reduced scarring [1].

Amongst these, percutaneous interventions, where instruments are inserted into the body through the skin, are gaining in popularity. The most common of these is needle insertion into soft tissue, used in inoculation, blood sampling, brachytherapy, biopsy, anaesthesia, etc. Here, the efficacy of treatment and the ability to perform a diagnosis are highly dependent on the accuracy of the insertion.

Currently, percutaneous procedures are carried out with rigid needles, however these have several limitations. Specifically, they can only perform straight trajectory insertions, so obstacles can limit or block access to the target site. Additionally, the needle and surrounding tissue may deform during insertion, which can cause the target to no longer lie on the needle path.

Steerable needles have been developed to address these challenges and, as outlined by [2], can take on a variety of different designs. The steering mechanisms are classified into seven different categories: base manipulation [3], bevel-tip (with and without pre-curve) [4]–[7], precurved stylet [8], active cannula [9], [10], programmable bevel-tip [11], [12], tendon actuated tip [13], [14], and most recently, optically controlled needle [15].

Crucial to accurately steering these needles, is the ability to model their interaction with the surrounding tissue. A model of the needle motion can be used to

1) simulate the system behavior;
2) evaluate and improve control strategies (see, for instance, model-based design method);
3) inform path-planning algorithms on the feasibility of given trajectories; and

Manuscript received June 22, 2018; accepted October 2, 2018. Date of publication December 11, 2018; date of current version April 2, 2019. This paper was recommended for publication by Associate Editor C. Bergeles and Editor P. Dupont upon evaluation of the reviewers' comments. This work was supported by both the European Commission under Grant 688279 and the EPSRC under Grant EP/M506345/1. *(Corresponding author: Ferdinando Rodriguez y Baena.)*

The authors are with the Mechatronics In Medicine Laboratory, Department of Mechanical Engineering, Imperial College London, London SW7 2AZ, U.K. (e-mail: t.watts14@imperial.ac.uk; r.secoli@imperial.ac.uk; f.rodriguez@imperial.ac.uk).

Color versions of one or more of the figures in this paper are available online at http://ieeexplore.ieee.org.

Digital Object Identifier 10.1109/TRO.2018.2879584

4) predict how design modifications may affect needle behavior.

Modeling of needle insertion into soft tissue is a challenging, and widely researched topic [2], with applications beyond needle steering, including realistic haptic rendering for surgical training. A comprehensive model should simultaneously consider needle deflection, tool-tissue interaction forces, and tissue deformation. Finite element (FE) analysis [16], [17], beam theory [18], [19], and spring foundations [20] have all been used to derive dynamic models for steerable needles. However, the complexity of these models means they are often not suitable for in-the-loop applications, which prevents their use in control strategies, and the high number of parameters introduced means they are often loosely constrained [21]. The much simpler kinematic, nonholonomic, bicycle model has been shown to provide a good fit to experimental testing conducted with a bevel-tip needle [7] and has also been considered for modeling the Programmable Bevel-tip Needle (PBN) [22]. It is, however, a phenomenological model, and so does not explicitly account for needle design parameters or tissue properties; the model parameters are found through regression.

The PBN, originally inspired by the ovipositor (egg-laying tube) of parasitic wasps [23], comprises multiple slender segments. These are held together by the "interlocking mechanism," which constrains relative motion to the axial direction. By controlling the relative insertion of segments, as shown in Fig. 1, the shape of the needle tip can be continuously "programmed" during insertion. The needle tip shape affects the interaction with the surrounding soft-tissue, and the resultant steering of the needle, as has been demonstrated in previous experimental trials [24]. One of the key advantages of the PBN's steering mechanism, when compared with the popular bevel-tip needle, is that it does not rely on transmission of torque from base to tip. It can therefore be manufactured from a much more compliant material, which allows greater steering ability in softer tissues (e.g., brain) and makes it more suitable for long-term implantation, as is required for chronic treatment.

To date, the control strategy for PBNs has assumed a linear model with adaptive compensation for unknown nonlinearities [25], [26]. However, to improve existing control strategies and inform future design decisions, the highly nonlinear relationship between the needle tip shape and steering needs to be better understood.

This paper presents a mechanics-based steering model for PBNs, which is suitable for in-the-loop application. An assumed tool-tissue interaction force is applied to a needle tip deflection model, which considers the multisegment structure as a set of multiple cantilevered Euler–Bernoulli beams. The model is validated, initially via a set of FE simulations, and subsequently through experimental trials with the first medical-grade and clinically sized PBN, the manufacture of which is also described herein. In this paper, the needle's ability to steer in any direction is also demonstrated for the first time.

This paper is arranged as follows. In Section II, the PBN steering model is presented and subsequently analyzed, to understand how needle design parameters affect steering characteristics. In Section III, results from FE simulations are compared with the model predictions. Section IV presents results from a series of experimental insertions, with a 4-segment, medical grade, 2.5 mm outer diameter PBN, from which best-fit model parameters are found and the model-predictive capability evaluated. In Section V, an open-loop three-dimensional (3-D) simulated trajectory is demonstrated with our conclusions given in Section VI.

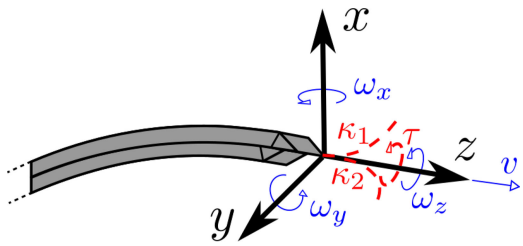

Fig. 2. Body frame coordinates shown for a PBN. Angular and linear velocities, $\omega_x, \omega_y, \omega_z$, and v are shown along with the corresponding curvatures κ_2, κ_1, and torsion τ. These can be used to describe the twist motion of a steerable needle, given in (3). For a PBN, it is assumed that $\tau \approx 0$.

II. Programmable Bevel-Tip Needle Model

The modeling of the PBN progresses as follows. Initially, in Section II-A, we consider the motion of steerable needles, and present the twist vector for a PBN, which motivates the subsequent model. Section II-C sets out a permissibility condition, which the needle tip shape must satisfy during operation. Sections II-D and II-E present the proposed force and Euler–Bernoulli beam deflection model, respectively, which together form the steering model. Section II-F considers how the model parameters, such as number of segments or cross-section design, affect the model-predicted needle behavior.

A. Steerable Needle Motion

The instantaneous linear and angular velocities of a rigid body can be conveniently described by a twist $\boldsymbol{\xi} \in \mathfrak{se}(3)$ [27]. A general twist is represented by a vector, defined as follows:

$$\boldsymbol{\xi} = \begin{bmatrix} \boldsymbol{\omega} \\ \boldsymbol{v} \end{bmatrix}_{6\times 1}$$

with three elements for angular and linear velocities, denoted by vectors $\boldsymbol{\omega}$ and $\boldsymbol{v}$, respectively. The twist motion for a steerable needle tip is most conveniently expressed in body frame coordinates, as shown in Fig. 2. A kinematic model of steerable needle motion is subject to Pfaffian constraints on the linear velocity

$$v_x = 0, \quad v_y = 0, \quad v_z = \frac{ds}{dt} = v$$

where s is the path length. If the pose of the tip frame is described with respect to a spatial reference frame by a 4×4 homogeneous matrix $\mathbf{T}_t \in SE(3)$

$$\mathbf{T}_t = \begin{bmatrix} \mathbf{R}_t & \mathbf{p}_t \\ 0_{1\times 3} & 1 \end{bmatrix} \tag{1}$$

where $\mathbf{R}_t = [\hat{\mathbf{e}}_\mathbf{x}\ \hat{\mathbf{e}}_\mathbf{y}\ \hat{\mathbf{e}}_\mathbf{z}]$ describes the tip orientation and $\mathbf{p}_t$ the tip position, then the instantaneous body-frame velocities v_i, ω_i can be recovered from the twist matrix $\hat{\boldsymbol{\xi}}^{\boldsymbol{b}}_{\boldsymbol{\Omega}} \in \mathfrak{se}(3)$

$$\hat{\boldsymbol{\xi}}^{\boldsymbol{b}}_{\boldsymbol{\Omega}} = \begin{bmatrix} 0 & -\omega_z & \omega_y & v_x \\ \omega_z & 0 & -\omega_x & v_y \\ -\omega_y & \omega_x & 0 & v_z \\ 0 & 0 & 0 & 0 \end{bmatrix} = \mathbf{T}_t^T \frac{d\mathbf{T}_t}{dt}. \tag{2}$$

In an analogous fashion, the instantaneous curvatures and torsion of the body can be described by $\hat{\boldsymbol{\xi}}^{\boldsymbol{b}}_{\boldsymbol{K}} \in \mathfrak{se}(3)$

$$\hat{\boldsymbol{\xi}}^{\boldsymbol{b}}_{\boldsymbol{K}} = \begin{bmatrix} 0 & -\tau & \kappa_1 & 0 \\ \tau & 0 & \kappa_2 & 0 \\ -\kappa_1 & -\kappa_2 & 0 & 1 \\ 0 & 0 & 0 & 0 \end{bmatrix} = \mathbf{T}_t^T \frac{d\mathbf{T}_t}{ds}$$

such that the curvatures κ_1 and κ_2 describe the change of the tangent vector $\hat{\boldsymbol{e}}_{\boldsymbol{z}}$ in the $\hat{\boldsymbol{e}}_{\boldsymbol{x}}$ and $\hat{\boldsymbol{e}}_{\boldsymbol{y}}$ directions, as defined in the body-attached frame. The torsion τ describes the rotation of $\hat{\boldsymbol{e}}_{\boldsymbol{x}}$ and $\hat{\boldsymbol{e}}_{\boldsymbol{y}}$ about the tangent vector. Assuming nonzero ds and dt such that both $\hat{\boldsymbol{\xi}}^{\boldsymbol{b}}_{\boldsymbol{\Omega}}$ and $\hat{\boldsymbol{\xi}}^{\boldsymbol{b}}_{\boldsymbol{K}}$ exist, simple application of the chain rule shows

$$\hat{\boldsymbol{\xi}}^{\boldsymbol{b}}_{\boldsymbol{\Omega}} = \mathbf{T}_t^T \frac{d\mathbf{T}_t}{dt} = \mathbf{T}_t^T \frac{d\mathbf{T}_t}{ds}\frac{ds}{dt} = v\,\hat{\boldsymbol{\xi}}^{\boldsymbol{b}}_{\boldsymbol{K}}$$

for $v \neq 0$. The general form for the body-frame twist $\boldsymbol{\xi}^b_G$ of a steerable needle tip can therefore be expressed

$$\boldsymbol{\xi}^b_G = \begin{bmatrix} \omega_x \\ \omega_y \\ \omega_z \\ v_x \\ v_y \\ v_z \end{bmatrix} = v \begin{bmatrix} -\kappa_2 \\ \kappa_1 \\ \tau \\ 0 \\ 0 \\ 1 \end{bmatrix}. \tag{3}$$

As previously demonstrated [25], [26], the tip geometry of the PBN can be modified during insertion to affect a change in the curvatures κ_1 and κ_2. As the line of action of the needle-tissue interaction force passes through the insertion axis, the tip does not experience significant torsional moments, and therefore it is assumed that $\tau \approx 0$. Hence, the twist for the PBN $\boldsymbol{\xi}^b_P$, shown alongside the twist for an axially rotated bevel-tip needle $\boldsymbol{\xi}^b_B$ as reported by [28], is as follows:

$$\boldsymbol{\xi}^b_P = v \begin{bmatrix} -\kappa_2 \\ \kappa_1 \\ 0 \\ 0 \\ 0 \\ 1 \end{bmatrix}, \quad \boldsymbol{\xi}^b_B = v \begin{bmatrix} 0 \\ \kappa \\ \tau \\ 0 \\ 0 \\ 1 \end{bmatrix}. \tag{4}$$

Both twists lie within a 3-system of screws. The transformation for trajectory equivalence is the same as the transformation between the Frenet–Serret and parallel transport [29] frames

$$\tau = \frac{d}{ds}\tan^{-1}\frac{\kappa_2}{\kappa_1}$$
$$\kappa = \sqrt{\kappa_1^2 + \kappa_2^2}.$$

The bevel-tip needle has an additional constraint with respect to the PBN, in that the curvature κ is constant. This precludes a straight trajectory, which may only be approximately achieved via continuous rotation, to give a tight helical path.

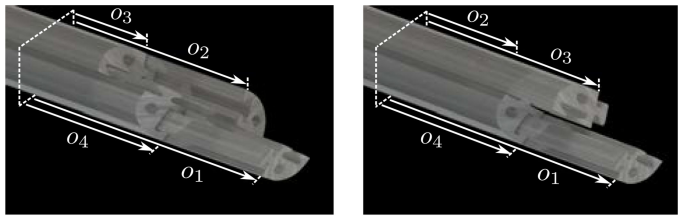

Fig. 3. Rendering of an $n = 4$ PBN tip, showing (a) a permissible configuration and (b) an impermissible configuration. During operation, it is crucial that the needle acts as a single flexible body. The tip configuration shown in (b) has two "free" segments that could drive the needle apart, and is therefore deemed impermissible.

B. Programmable Bevel-Tip Needle Operation

The tip shape of an n-segment PBN is determined by the relative positioning of the n segments, as shown in Fig. 3. For convenience, each segment's extension may be measured relative to a reference plane that moves with the needle tip. These distances are termed the segment offsets and together form an offset vector that describes the tip configuration $\boldsymbol{o} \in \mathbb{R}^n$. It should be noted that this representation has a single redundancy - the common-mode displacement of all segments. In the model presented here, this redundancy is given meaning, with the reference plane notionally describing the boundary between the needle tip, which controls steering, and the needle shaft, which has been shown to approximately follow the trajectory described by the tip, as in "follow-the-leader" deployment [9].

We can describe the relative positioning of the n segments with only $n-1$ variables. These are termed the relative segment offsets and together form a relative offset vector $\boldsymbol{\Theta} \in \mathbb{R}^{n-1}$, a minimal set of coordinates. They are defined by the following change of variables.

For $i = 1$ to $n-1$

$$\Theta_i = o_{i+1} - o_1$$
$$l = \max o_i \tag{5}$$

where l is a model parameter, termed the tip length (e.g., $l = o_1$ in Fig. 3).

The problem of determining the trajectory evolution of a PBN is therefore equivalent to finding the function f that maps from the relative offset vector $\boldsymbol{\Theta} \in \mathbb{R}^{n-1}$, to the curvature

components κ_1 and κ_2, as defined in (4)

$$\boldsymbol{\kappa}_P = \begin{bmatrix} \kappa_1 \\ \kappa_2 \end{bmatrix} = f(\boldsymbol{\Theta}, \boldsymbol{\mu}) \tag{6}$$

where $\boldsymbol{\mu}$ is a vector of model parameters and we define $\boldsymbol{\kappa}_P \in \mathbb{R}^2$, the curvature vector.

The relationship described by the function $f(\boldsymbol{\Theta}, \boldsymbol{\mu})$ is highly dependent on the complex tool-tissue interaction at the tip. The interaction has been studied and modeled in 2-D using FE methods [16], but the analysis is computationally costly and therefore not suitable for in-the-loop applications.

By making assumptions about the nature of the force interaction between the needle and surrounding tissue, and using linear Euler–Bernoulli beam theory, we develop a simplified steering model. The model predicts PBN steering for low speed tissue traversal. Therefore, initial tissue puncture is not considered and needle insertion velocity is assumed to be sufficiently low, such that inertial and viscoelastic effects may be ignored and the process is quasi-static.

C. Permissibility Condition for Tip Configuration

We first consider restrictions on the model input, which is the offset vector that defines the shape of the needle tip. During operation, it is crucial that the needle acts as a single, flexible body. This requires that a tip configuration satisfies a permissibility condition, which can be intuitively understood by considering the two tip configurations in Fig. 3, shown for the case $n = 4$.

For an n-segment programmable bevel-tip needle, the permissibility condition for an offset vector $\boldsymbol{o}$ is derived below. Note that the permissibility of a relative offset vector $\boldsymbol{\Theta}$ may be evaluated by first converting to an offset vector $\boldsymbol{o}$ via the (reverse) change of variables in (5), with arbitrary l.

First, consider an index set I for the needle segments, defined as

$$I = \{1, \ldots, i, \ldots, n \mid n \in \mathbb{Z}^+\}.$$

The corresponding set of offsets O describes the tip configuration

$$O = \{o_i \mid i \in I, o_i \in \mathbb{R}\}.$$

For segment i, the clockwise neighboring segment is denoted i^+, given by

$$i^+ = i \pmod n + 1\ ,\ i^+ \in I.$$

Define a_i, b_j, c_k as follows:

$$a_i = \text{sgn}(o_{i^+} - o_i)$$

$$b_j = a_{j^+} - a_j$$

$$c_k = \begin{cases} 1, & \text{if } b_k = -2 \\ 0, & \text{otherwise.} \end{cases}$$

If $c_k = 1$, the segment corresponding to k^+ is termed "free". Physically, this corresponds to a segment for which the tip is further extended than its neighboring segments. For an offset configuration to be permissible, it must contain at most one free segment, and therefore the permissibility condition is[1]

$$\sum_{k=1}^{n} c_k \leqslant 1.$$

It is worth noting that impermissible tip configurations only exist for cases $n \geqslant 4$.

This permissibility condition must be satisfied to ensure the needle acts as a single body during insertion, which is required for the following proposed model.

D. Force Model

A comprehensive model for the forces generated by the needle-tissue interaction would require a highly computationally expensive, 3-D FE simulation, accounting for tissue hyperelasticity and crack dynamics. However, such a model would not be suitable for the desired in-the-loop application. Here, the loading is assumed to take a particular form, for which best-fit model parameters are to be found. The form is based on prior needle-tissue interaction force studies and physical intuition.

Assumptions:

1) The tool-tissue interaction forces are expected to act as a distributed load, predominantly upon the beveled faces of the segment tips. Since we are not interested in local deformation of the bevel faces, according to Saint–Venant's principle, we consider the distributed loads equivalent to point forces acting normal to each segment's bevel face.
2) Since the beam deflection model presented in the following section only considers transverse deflection, only transverse force components are of interest.
3) The forces acting on a needle during insertion into soft tissue contain contributions from tissue deformation, tissue cutting and friction at the needle-tissue interface [30]. Friction forces act predominantly in the axial direction, and are therefore disregarded. The forces acting on the beveled faces are therefore assumed to comprise only deformation and cutting components. The assumed form of these contributions is discussed.
4) The loading on the tip depends only on the tip configuration, described by the relative offsets, and not the tip deflection. This requires that the deflection of the tip is assumed to be small, such that higher-order terms due to force/deflection coupling are not significant.

As the needle is inserted, each segment displaces the tissue directly ahead of it. As all segments have the same frontal area, the deformation force contribution is assumed to act equally on each segment tip. On the other hand, the cutting force contribution is expected to act with a greater proportion on the leading segment tip, which works greatest to propagate the crack ahead

[1]Compactly, the permissibility of a given offset configuration may be evaluated by the following Mathworks MATLAB2016b expression, which returns 1 if a given configuration $\boldsymbol{o}$ is permissible, and 0 if it is impermissible

$$\texttt{sum}(\texttt{difc}(\texttt{sign}(\texttt{difc}(\boldsymbol{o}))) == -2) <= 1 \tag{7}$$

where `sum` and `sign` are MATLAB functions and `difc` is the circular difference function, i.e., $\texttt{difc}([x_1, x_2, x_3]) = [x_1 - x_3, x_2 - x_1, x_3 - x_2]$

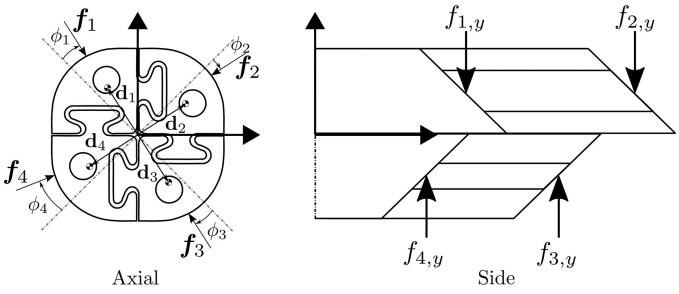

Fig. 4. Forces $\boldsymbol{f}_i$ are shown acting on the needle tip of an $n = 4$ PBN. The axial view shows how a force angle deviation ϕ_i affects the direction of force application on segment i. The positions of the segment centroids which correspond to the segment neutral axes are shown, denoted $\boldsymbol{d}_i$. The side view shows the forces acting on the beveled segment faces. The z-component of the force is ignored due to the assumption of pure transverse deflection. Note the coordinate system, denoted η, is different to that of Fig. 2, and is attached to the base of the needle tip.

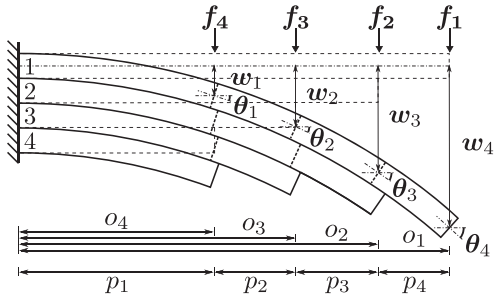

Fig. 5. Deflections $\boldsymbol{w}_j$ and rotations $\boldsymbol{\theta}_j$ for portions $j = 1$ to n, of length p_j, are shown in a 2-D representation of the 3-D beam-bending deflection model for the case $n = 4$. o_i are the offsets corresponding to the segments i, and the forces $\boldsymbol{f}_i$ are the respective tip loads, shown acting on the undeformed needle tip. Note: the magnitude of deflection is exaggerated for the sake of clarity.

of the needle. Consider a second (nonleading) segment: when aligned with the leading segment, it should bear an equal force, but as it is withdrawn, its contribution is expected to drop, approaching zero in the limit. A natural candidate for the cutting contribution is therefore an exponential function, which decays with distance from the leading segment tip.

As a result, the transverse tip force magnitude F_i, acting upon segment i, is assumed to take the following form:

$$F_i = F_p \frac{1}{n} + F_c \frac{e^{-\frac{l-o_i}{l_c}}}{\sum_{i=1}^{n} e^{-\frac{l-o_i}{l_c}}} \tag{8}$$

where $l - o_i$ is the distance of segment i from the furthest extended segment. F_p and F_c are the total deformation and cutting force acting on the tip, respectively, and l_c is the cutting length constant that effects how the cutting force is distributed along the needle tip. F_p, F_c, and l_c are all model parameters, that are expected to depend on the surrounding tissue properties and shape of the segment tips.

It has proved hard to reliably control the angle of the bevel plane when fabricating PBNs. Therefore, a force angular deviation term ϕ_i is introduced for each segment i. The direction of the applied force on segment i is described by β_i, as shown in Fig. 4

$$\beta_i = \frac{\pi}{n}(2i - 3) + \phi_i.$$

The transverse tip force acting on segment i, as shown in Fig. 4, is given by the vector $\boldsymbol{f}_i$

$$\boldsymbol{f}_i = \begin{bmatrix} f_{i,x} \\ f_{i,y} \end{bmatrix} = \mathbf{R}_{\beta_i} \begin{bmatrix} 0 \\ -F_i \end{bmatrix} = -F_i \begin{bmatrix} \sin(\beta_i) \\ \cos(\beta_i) \end{bmatrix} \tag{9}$$

where $\mathbf{R}_{\beta_i} \in SO(2)$ denotes the matrix[2] which corresponds to a clockwise rotation for an angle β_i.

E. Deflection Model

With the force distribution established, we now calculate the resultant needle tip deflection. This will determine the model-predicted curvature vector.

[2]For the following sections, all rotation matrices are defined similarly

Assumptions:

1) The deflection of a single bending segment may be modeled as an Euler–Bernoulli beam. It is therefore assumed that the beam undergoes small deflections and is sufficiently slender, such that shear strain effects are negligible. The cross-section is assumed to be constant: the effect due to slight taper from the bevel face is, thus, also assumed to be negligible.
2) The axial load is assumed to be negligible as the axial stiffness of the needle is much greater than the bending stiffness. The axial component of the tip force and friction acting along the needle shaft are therefore discarded and only bending in the transverse plane is considered.
3) The friction force acting between segments is negligible (see Section IV-A), such that no shear forces are transferred between segments. Each segment will therefore bend about its own neutral axis.
4) The interlocking mechanism constrains relative transverse motion of the segments. In tandem with the slenderness and small deflection assumptions stated in (1), each of the comprising segments therefore experience the same curvature at any given cross-section of the tip.

In order to calculate the deflection of the needle tip under the external loading of (9), the tip is partitioned into portions of constant cross-section. Each portion j has length $p_j \in \mathbb{R}$ and corresponding second moment of area tensor $\widetilde{\mathbf{I}}_j \in \mathbb{R}^{2\times 2}$. The deflection $\boldsymbol{w}_j \in \mathbb{R}^2$ and rotation $\boldsymbol{\theta}_j \in \mathbb{R}^2$ are shown in Fig. 5. It will be convenient to define the set J_j of segments comprising portion j.

The internal reactions are calculated at the portion boundaries. The shear force $\boldsymbol{s}_j \in \mathbb{R}^2$ and bending moment $\boldsymbol{m}_j \in \mathbb{R}^2$, as shown in Fig. 6, are found by balancing internal with external loads. Note the rotation $\mathbf{R}_{\frac{\pi}{2}}$ is necessary so that a force acting in the x-direction generates a moment about the y-axis and vice versa

$$\boldsymbol{s}_j = \begin{bmatrix} s_{j,x} \\ s_{j,y} \end{bmatrix} = \sum_{J_j} \boldsymbol{f}_i \tag{10}$$

$$\boldsymbol{m}_j = \begin{bmatrix} m_{j,x} \\ m_{j,y} \end{bmatrix} = \sum_{J_j} \mathbf{R}_{\frac{\pi}{2}} \boldsymbol{f}_i \left(o_i - \sum_{k=1}^{j} p_k \right). \tag{11}$$

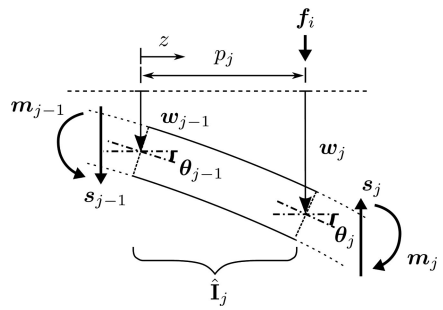

Fig. 6. Internal bending moment $\boldsymbol{m}_j$ and shear force $\boldsymbol{s}_j$ shown for portion j in a 2-D representation of a single portion. $\hat{\boldsymbol{I}}_j$ is the second moment of area tensor and z is the distance measured along the portion. Other parameters are as in Fig. 5.

For a general cross-section, the geometrical contribution to the bending stiffness is given by the second moment of area tensor

$$\mathbf{I} = \begin{bmatrix} I_{xx} & I_{xy} \\ I_{yx} & I_{yy} \end{bmatrix}$$

where I_{xx} and I_{yy} are the second moments of area about the centroidal perpendicular axes xx and yy, respectively, and $I_{xy} = I_{yx}$ is the corresponding product moment of area.

Assuming all segments have the same cross-section geometry, it is sufficient to calculate the second moment of area tensor for a single segment (e.g., I_1, the second moment area tensor for the first segment). The transformed second moment of area tensor for segment i, rotated by an angle γ_i, can therefore be calculated as

$$\gamma_i = \frac{2\pi}{n}(i-1)$$
$$\mathbf{I}_i = \mathbf{R}_{\gamma_i}\mathbf{I}_1\mathbf{R}_{\gamma_i}^T.$$

Considering the second assumption, the second moment of area tensor for portion j is given simply by the following sum:

$$\hat{\mathbf{I}}_j = \sum_{J_j} \mathbf{I}_i. \tag{12}$$

Considering the Euler–Bernoulli beam equation, the internal bending moment $\boldsymbol{m}$ at each point along a beam is related to the curvature $\boldsymbol{\kappa}$ as follows:

$$\boldsymbol{m} = \begin{bmatrix} m_x \\ m_y \end{bmatrix} = -E\mathbf{I}\boldsymbol{\kappa} = -E\mathbf{I}\begin{bmatrix} \kappa_x \\ \kappa_y \end{bmatrix} = E\mathbf{I}\mathbf{R}_{\frac{\pi}{2}}\frac{d^2\boldsymbol{w}}{dz^2}$$

where E is the Young's modulus, which together with the second moment of area tensor, forms the flexural rigidity tensor $E\boldsymbol{I}$. Rearranging yields

$$\frac{d^2\boldsymbol{w}}{dz^2} = \frac{1}{E}\mathbf{R}_{\frac{\pi}{2}}^T\mathbf{I}^{-1}\boldsymbol{m}. \tag{13}$$

For $0 \le z \le p_j$ measured along a single portion j, the bending moment $\boldsymbol{m}(z)$ is

$$\boldsymbol{m}(z) = \boldsymbol{m}_j + (p_j - z)\mathbf{R}_{\frac{\pi}{2}}\boldsymbol{s}_j. \tag{14}$$

Substituting (14) into (13), integrating twice with respect to z and applying continuity conditions at the portion boundaries, yields the expressions for the rotation $\boldsymbol{\theta}_j$ and deflection $\boldsymbol{w}_j$ of each portion

$$\boldsymbol{\theta}_j = \begin{bmatrix} \theta_{j,x} \\ \theta_{j,y} \end{bmatrix} = \left.\frac{d\boldsymbol{w}}{dz}\right|_{z=p_j}$$
$$= \boldsymbol{\theta}_{j-1} + \frac{p_j^2}{2E}\mathbf{R}_{\frac{\pi}{2}}^T\hat{\mathbf{I}}_j^{-1}\mathbf{R}_{\frac{\pi}{2}}\boldsymbol{s}_j + \frac{p_j}{E}\mathbf{R}_{\frac{\pi}{2}}^T\hat{\mathbf{I}}_j^{-1}\boldsymbol{m}_j \tag{15}$$

$$\boldsymbol{w}_j = \begin{bmatrix} w_{j,x} \\ w_{j,y} \end{bmatrix} = \boldsymbol{w}|_{z=p_j}$$
$$= \boldsymbol{w}_{j-1} + p_j\boldsymbol{\theta}_{j-1} + \frac{p_j^3}{3E}\mathbf{R}_{\frac{\pi}{2}}^T\hat{\mathbf{I}}_j^{-1}\mathbf{R}_{\frac{\pi}{2}}\boldsymbol{s}_j + \frac{p_j^2}{2E}\mathbf{R}_{\frac{\pi}{2}}^T\hat{\mathbf{I}}_j^{-1}\boldsymbol{m}_j \tag{16}$$

with fixed end boundary conditions applied at the tip base (zero rotation and deflection used by convention as curvature is independent of beam position and orientation)

$$\boldsymbol{\theta}_0 = \boldsymbol{w}_0 = \mathbf{0}_{2\times 1}. \tag{17}$$

From the deflection of the furthermost protruding segment tip $\boldsymbol{w}_n$, the average curvature of the needle tip $\hat{\boldsymbol{\kappa}}$ is calculated. This is the model prediction of the curvature vector $\boldsymbol{\kappa}_P$ in (6)

$$\hat{\boldsymbol{\kappa}} = \begin{bmatrix} \hat{\kappa}_1 \\ \hat{\kappa}_2 \end{bmatrix} = \frac{2}{l^2}\boldsymbol{w}_n. \tag{18}$$

In summary, the steering model follows the following steps, detailed above.

1) Check permissibility of tip configuration (7).
2) Evaluate force model to return forces acting on segments (9).
3) Identify needle portions.
4) Calculate shear force and bending moment at portion boundaries (10) and (11).
5) Calculate portion cross-section properties (12).
6) Evaluate Euler–Bernoulli beam equation to find tip displacement (15)–(17).
7) Return average curvature vector, calculated from tip displacement (18).

A single evaluation, run on a standard desktop PC,[3] takes an average of 34 ms.

F. Model Observations

As a first means of evaluating the model, the effects of varying the model parameters, summarized in Table I, are considered. Of particular interest are those model parameters that can be varied by design, namely: the number of segments n, the flexural rigidity $E\mathbf{I}_1$, and force angle deviations ϕ_i. Variation in each of the design parameters is considered, whilst the remaining model parameters are set to be the default values listed in Table I.

[3]Performed with a .mex file in Mathworks MATLAB2016b 64 bit, run on an Intel(R) Core(TM) i7-4770 CPU @3.40 GHz

TABLE I
MODEL PARAMETERS, RESPECTIVE UNITS AND DEFAULT VALUES

Model Parameter	Symbol	Units	Default Value
Number of segments	n	–	4
Flexural rigidity tensor	$E\mathbf{I}_1$	N mm^2	$\begin{bmatrix} 1 & 0 \\ 0 & 1 \end{bmatrix}$
Force angle deviations	$\phi_1, \ldots, \phi_n$	–	0
Tip length	l	mm	1
Deformation Force	F_p	N	1
Cutting Force	F_c	N	0
Cutting length constant	l_c	mm	1

1) Number of Segments n: The model presented is applicable to a general n-segment PBN. A comparison between the achievable curvatures for different n indicates the ability of different designs to steer.

Fig. 7 shows the range of achievable curvatures $\hat{\boldsymbol{\kappa}}$ for different n. The plots all exhibit rotational symmetry of order n, reflecting the rotational symmetry of the needle design. A single-segment needle ($n = 1$), has no ability to configure the tip, and is therefore limited to a single curvature. For a two-segment needle ($n = 2$), $\kappa_2 = 0$, and therefore the needle is constrained to curvature within a single plane. A three-segment needle ($n = 3$) is the minimum required to achieve steering in any desired direction. The maximum curvature achievable varies by direction, with the greatest achievable curvature corresponding to the single segment forward configurations. For cases with $n \geq 4$, there are multiple tip configurations that result in the same curvature vector $\hat{\boldsymbol{\kappa}}$, and again, the maximum achievable curvature is greatest for the single segment forward configurations.

2) Flexural Rigidity $E\mathbf{I}_1$: The flexural rigidity tensor $E\mathbf{I}_1$ describes the segment cross-section's resistance to bending. The Young's modulus E corresponds to the material property contribution, and the second moment of area tensor $\mathbf{I}_1$ corresponds to the geometric contribution.

For the special case where the flexural rigidity tensor is a scalar multiple of the identity matrix, the achievable curvature plot is symmetric within each quadrant, as shown in Fig. 7(c). The real second moment of area tensor for the segment cross-section of the 4-segment PBN, shown in Fig. 4, is calculated in Dassault Systèmes SolidWorks and used to generate Fig. 7(d)

$$\mathbf{I}_1 = \begin{bmatrix} 0.1082 & -0.0229 \\ -0.0229 & 0.2147 \end{bmatrix} \text{mm}^4.$$

In this case, the maximum curvatures, achieved in a single segment forward tip configuration, no longer lie in the 45° directions, due to the slight asymmetry in the segments' cross-section. There is also an increase in the variation of maximum curvature with direction, with a marked increase in the predicted curvature for the single segment forward directions.

3) Force Angle Deviations ϕ_i: The force angle deviations ϕ_i account for the variation of the tip force direction between segments. This arises due to variation in the angle of the bevel cut plane. For an ideal PBN, $\phi_i = 0$ for all i, and the achievable curvature plot has rotational symmetry, as shown in Fig. 7(c) and (d). Fig. 7(e) shows the effect of a nonzero force angle deviation, specifically $\phi_1 = 20°$. It produces a quadrant specific skew and rotational symmetry is lost.

III. FE SIMULATIONS

To evaluate the multibeam deflection model, FE simulations using SIMULIA Abaqus FEA 6.14, were performed on the geometry of our PBN, for the cases with $n = 3, 4$. Observed deflections were compared with model-predicted deflections for equivalent loading conditions: an equal pressure force applied to each segment tip; and equivalent design parameters: same Young's modulus and second moment of area tensor.

A. Method

The segments of the PBN were meshed with linear hexahedral elements of type C3D8R. A mesh convergence study confirmed stability for deformation with respect to mesh size. For the analysis, the interaction between segments is frictionless and the material is linear elastic with Young's modulus E and Poisson's ratio ν. The second moment of area tensor for a segment's cross-section is $\mathbf{I}$. The loading at the tip of each segment is provided by a uniform pressure p, acting on the beveled faces of area A, which are cut at an angle α.

During the simulations, all segments were subjected to the same tip loading. An explicit analysis was performed with SIMULIA Abaqus, using the parameters reported in Table II. The analysis was quasi-static, therefore inertial and time-dependent effects are negligible. The deflection was recorded for the tip node of the furthermost extended segment.

For the comparison, the needle model (see Section III-C) parameters E and $\mathbf{I}_1$ are those given in Table II. The equivalent transverse tip force magnitude acting on segment i is $F_i = pA\cos(\alpha)$, with zero force angle deviations (i.e., $\phi_i = 0$). The tip length for all offset configurations is $l = 20$ mm. The model predicted tip deflections $\boldsymbol{w}_n$ are calculated for the same tip configurations, listed in Table III.

B. Results and Discussion

The tip configurations used for the FE simulations are reported in Table III, along with a visual depiction of the needle tip deflections. The tip node deflection for each configuration, $\boldsymbol{w}_n$, is shown in Fig. 8, along with the deflection path as the load on each segment is increased from 0 to F_i.

The root-mean-square deviation (RMSD) between the FE simulation and the model predicted values was 0.1664 mm and 0.2636 mm for the cases $n = 3$ and $n = 4$, respectively. Fig. 8 shows the increased deflection for offset configurations with either a single or two segments forward. Additionally, asymmetry due to the needle geometry is observed in both sets of results. The tip deflection paths are *"quasi-linear"* with nonlinearity becoming a greater factor as the deflection increases.

Sources of discrepancy between the model predictions and FE results are attributed to the following:

1) nonsmall deflection: not considered in linear Euler–Bernoulli, which assumes $\frac{dw}{dz} \ll 1$;

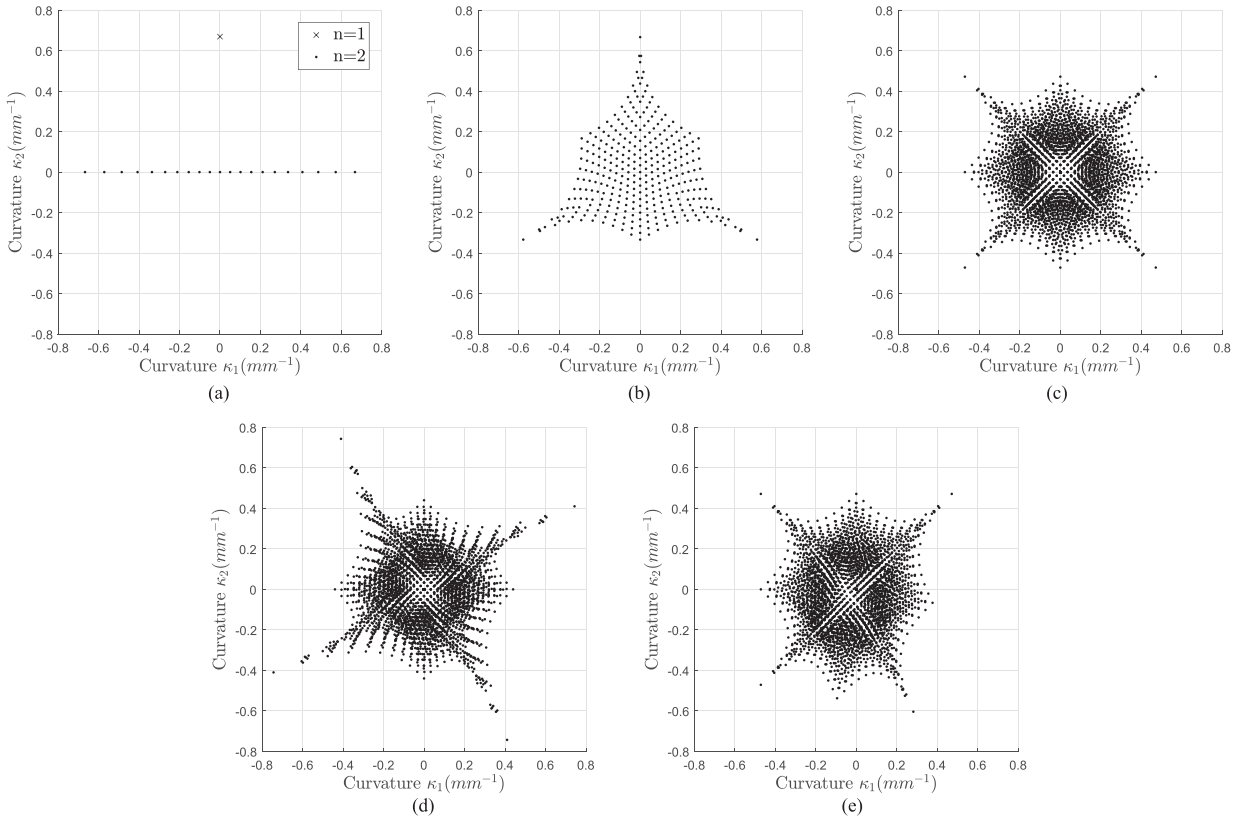

Fig. 7. Model-predicted achievable curvatures are plotted for different design parameters. (a) $n = 1, 2$. (b) $n = 3$. (c) $n = 4$. (d) Nonidentity flexural rigidity tensor $E\boldsymbol{I}_1$ (exact value given in the text). (e) $\phi_1 = 20°$. They are generated by discretizing the space of all permissible tip configurations into 0.1 mm steps. The other model parameters are set to the default values given in Table I.

TABLE II
PARAMETERS USED IN THE FE SIMULATION

Parameter	Value (units)
E	15 MPa
ν	0.33
p	0.005 N mm^{-2}
α	30°
for n=3	
$\mathbf{I}_1$	$\begin{bmatrix} 0.2582 & -0.1155 \\ -0.1155 & 0.3120 \end{bmatrix}$ mm^4
A	3.015 mm^2
F_i	0.0131 N
for n=4	
$\mathbf{I}_1$	$\begin{bmatrix} 0.1082 & -0.0229 \\ -0.0229 & 0.2147 \end{bmatrix}$ mm^4
A	2.813 mm^2
F_i	0.0095 N

2) transverse shear strain: not considered in linear Euler–Bernoulli beam theory, which assumes slender beams (i.e., length $\gg$ width);
3) torsion: the force acting on each segment does not necessarily act through the shear center, and therefore torsion may be induced in the segments;
4) nonlinearities: these arise due to nonperfect transmission of stresses between segments, particularly at cross-section discontinuities; and
5) cross-section variation: at the tip of each segment, the bevel causes a gradual change in cross-section, whereas the deflection model assumes constant cross-section beams.

The first-order agreement is satisfactory. With the strong assumptions made in the force model, we expect that the magnitude of the errors seen here in the deflection model to be small in comparison. The expected magnitude of these errors in the context of the experimental trials are discussed in Section IV-C.

IV. EXPERIMENTAL TRIALS

An extensive series of experimental needle insertions were performed to evaluate the needle's steering ability and the accuracy of the proposed model. These were performed by following a similar protocol to our previous works [22], [23], [31].

The steering ability is quantified by the maximum achievable curvature, the reciprocal of the minimum radius of curvature. For an environment containing obstacles, a greater maximum achievable curvature enables access to a larger proportion of the workspace [32]. For the steering ability evaluation, a 10% by weight bovine gelatin (Chef William Powdered Gelatine) was used, as in the previous evaluation of flexure-tip steerable needles [33]. A single segment forward configuration was used with an offset of 20 mm.

The steering model predicts the curvature vector $\boldsymbol{\kappa}_P$ of a PBN for a given tip configuration, determined by the relative offset vector $\boldsymbol{\Theta}$. To evaluate the proposed model, insertions were per-

TABLE III
FE SIMULATION RESULTS, SHOWING AXIAL VIEW OF PBN TIP DEFLECTIONS, FOR CASES $n = 3, 4$

Tip configuration (mm) $\{o_1, o_2, o_3, o_4\}$	Deflection	Tip configuration (mm) $\{o_1, o_2, o_3\}$	Deflection
A4: $\{20, 20, 10, 10\}$		A3: $\{20, 20, 10\}$	
B4: $\{20, 18, 10, 10\}$		B3: $\{20, 18, 10\}$	
C4: $\{20, 16, 10, 10\}$		C3: $\{20, 16, 10\}$	
D4: $\{20, 14, 10, 10\}$		D3: $\{20, 14, 10\}$	
E4: $\{20, 12, 10, 10\}$		E3: $\{20, 12, 10\}$	
F4: $\{20, 10, 10, 10\}$		F3: $\{20, 10, 10\}$	
G4: $\{20, 10, 10, 12\}$		G3: $\{20, 10, 12\}$	
H4: $\{20, 10, 10, 14\}$		H3: $\{20, 10, 14\}$	
I4: $\{20, 10, 10, 16\}$		I3: $\{20, 10, 16\}$	
J4: $\{20, 10, 10, 18\}$		J3: $\{20, 10, 18\}$	
K4: $\{20, 10, 10, 20\}$		K3: $\{20, 10, 20\}$	

An equal load is applied to each segment tip, as specified in Table II. The resultant tip deflections for each of the configurations are also presented in Fig. 8.

formed for a range of tip configurations in a 6% by weight bovine gelatin. The lower concentration of gelatin is more readily dissolved and therefore a more consistent set of phantoms can be generated for the model evaluation trials. Uniaxial compression tests were performed on three gelatin samples for each concentration. The shear moduli, obtained through an incompressible Neo–Hookean hyperelastic model fit, were measured to be (7.72 ± 0.08) kPa for the 10% sample and (3.05 ± 0.09) kPa for the 6% sample, which we believe to be an acceptable first approximation for human white matter [34].

A. Manufacture of a Medical-Grade Programmable Bevel-Tip Needle

The experimental trials were performed with a new 4-segment PBN. The fully assembled needle design has an outer diameter of 2.5 mm, which is within the range appropriate for neurological instruments (e.g., RAUMEDIC NEUROVENT [35]). The segments are manufactured via extrusion of medical-grade, plasticized poly(vinyl chloride) with 86 Shore "A" hardness, by Xograph Healthcare Ltd. To ensure low friction sliding between segments, the needle segments are nanocoated with poly(para-xylylene).

Fig. 9(a) shows the cross-section of a single segment, viewed under a microscope. Each segment has a male and female part of the interlocking mechanism, which connect to the neighboring segments. A single 0.3 mm outer diameter lumen provides a channel from base to tip of each needle segment, which could be used for a variety of clinical applications, ranging from drug delivery and cyst evacuation, to optical based diagnostic sensing.

The tip of each segment is ground to form a beveled face at approximately 30° from the neutral axis. The plane of the bevel is approximately aligned, such that the surface normal passes through the central axis of the needle. Due to the flexible nature of the material, an accurate alignment of the bevel plane is difficult to achieve. The fully assembled PBN tip is shown in Fig. 9(b).

B. Method

1) Experimental Design: The gelatin phantoms were kept at a controlled room temperature of (21–22) °C. Deviations from this temperature can significantly affect the mechanical properties of the gelatin.

A set of 24 tip configurations, listed in Table IV, were used for the insertions. Of these, 16 were used for performing the model fit, and the remaining eight for model validation. Single and two forward configurations achieve steering in all of the eight principal directions, and have been used in previous studies [24]. Additionally, eight "mixed" configurations were selected, with two nonaligned extended segments. These are chosen to provide a sufficient set of data to fit the cutting model parameters, as identified in Section II-D. For model validation, eight "randomized" configurations were generated, and checked to ensure that they satisfy the permissibility condition of Section II-C.

For each tip configuration, at least seven insertions were performed. To mitigate the effect of varying gelatin properties between boxes, the trials were performed in a randomized order. The needle's trajectory was recorded using a calibrated stereo camera pair.[4]

2) Needle Insertion: The insertion of the four segments was driven by a robotic system formed of four linear actuators, at a predefined speed of 1 mm$\cdot$ s^{-1}, as in previous studies [22], [24]. The experimental setup is shown in Fig. 10.

The PBN was initially inserted 20 mm into the phantom-brain gelatin, with all segments aligned. As the furthermost extended segment was held stationary, the other segments were driven to form the desired tip configuration. All linear actuators were then driven in unison for a subsequent insertion of 100 mm.

[4]The stereo images were captured with two Logitech C920 HD Pro webcams at fixed focal lengths. A ray tracing algorithm accounts for refraction at the air-gelatin interface. A calibration test using a known geometry, positioned at different locations and depths within the relevant workspace, showed RMS positioning accuracy of ± 0.80 mm, comparable to the commonly used NDI Aurora EM tracker.

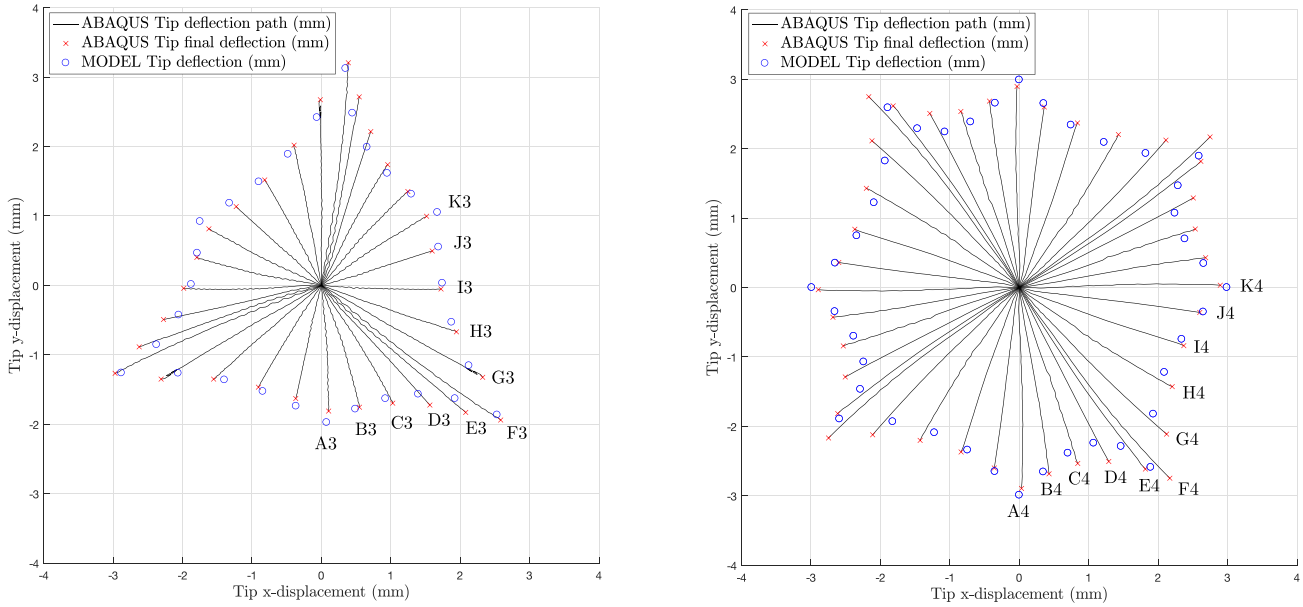

Fig. 8. Comparison between FE simulation results and model predictions for the deflection of a PBN tip. (a) Case $n = 3$. (b) Case $n = 4$. Results are plotted for the tip configurations listed in Table III, and rotational symmetry used to complete the plot for all directions. The deflection path shows the displacement of the tip node as the forces acting on the segments are increased from 0 to F_i. The RMSD between the FE simulation and the model predicted values was 0.1664 mm and 0.2636 mm for the cases $n = 3$ and $n = 4$, respectively.

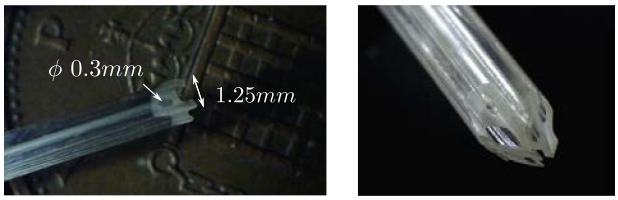

Fig. 9. Microscope images of the 2.5 mm outer diameter PBN. (a) Single segment showing the interlocking mechanism and lumen. (b) Tip of the fully assembled PBN with all segments aligned.

3) Curvature Estimation: The estimation of the curvature vector $\boldsymbol{\kappa}_{\text{exp}}$ from the resultant trajectory was calculated via the following steps.

1) The best-fit steering plane was found using principal components analysis, based on singular value decomposition.
2) The trajectory was orthogonally projected onto the best-fit steering plane.
3) The Hyperfit circle-fitting method [36] was used to estimate the best-fit radius R_{exp} from which the curvature magnitude $\kappa_{\text{exp}} = 1/R_{\text{exp}}$ was calculated.
4) The angle of insertion Φ_{exp} is measured between the best-fit steering plane and the horizontal plane in which the needle is initially inserted.

The experimental curvature vector, measured for a given insertion, is therefore

$$\boldsymbol{\kappa}_{\text{exp}} = \kappa_{\text{exp}} \begin{bmatrix} \cos\left(\Phi_{\text{exp}}\right) \\ \sin\left(\Phi_{\text{exp}}\right) \end{bmatrix}.$$

TABLE IV
TIP CONFIGURATIONS USED IN EXPERIMENTAL TRIALS AND THE CORRESPONDING RELATIVE OFFSET VECTORS $\boldsymbol{\Theta}$

Tip configuration	Relative offset vector (mm) $\{\Theta_1, \Theta_2, \Theta_3\}$	Description	Model use
N	$\{0, 20, 20\}$	Two Forward	Fitting
E	$\{20, 20, 0\}$	Two Forward	Fitting
S	$\{0, -20, -20\}$	Two Forward	Fitting
W	$\{20, 20, 0\}$	Two Forward	Fitting
NE	$\{0, 0, 20\}$	Single Forward	Fitting
SE	$\{-20, -20, -20\}$	Single Forward	Fitting
SW	$\{20, 0, 0\}$	Single Forward	Fitting
NW	$\{0, 20, 0\}$	Single Forward	Fitting
NNE	$\{0, 16, 20\}$	Mixed	Fitting
ENE	$\{-12, -12, 8\}$	Mixed	Fitting
ESE	$\{-20, -20, -8\}$	Mixed	Fitting
SSE	$\{-4, -20, -20\}$	Mixed	Fitting
SSW	$\{2, -18, -18\}$	Mixed	Fitting
WSW	$\{20, 14, 0\}$	Mixed	Fitting
WNW	$\{14, 20, 0\}$	Mixed	Fitting
NNW	$\{0, 20, 18\}$	Mixed	Fitting
R1	$\{5, 13, 14\}$	randomized	Validation
R2	$\{17, 16, 7\}$	randomized	Validation
R3	$\{-13, -7, 3\}$	randomized	Validation
R4	$\{4, -3, -15\}$	randomized	Validation
R5	$\{2, -4, -2\}$	randomized	Validation
R6	$\{1, -12, -6\}$	randomized	Validation
R7	$\{4, 6, 7\}$	randomized	Validation
R8	$\{-1, -1, 13\}$	randomized	Validation

16 configurations are used for the model fit, with a further 8 randomized configurations used for validation.

C. Results and Discussion

1) Steering Ability: The maximum curvature achieved was 0.0192 ± 0.001 mm^{-1}, with a representative insertion shown in Fig. 10. Care should be taken when making direct comparison

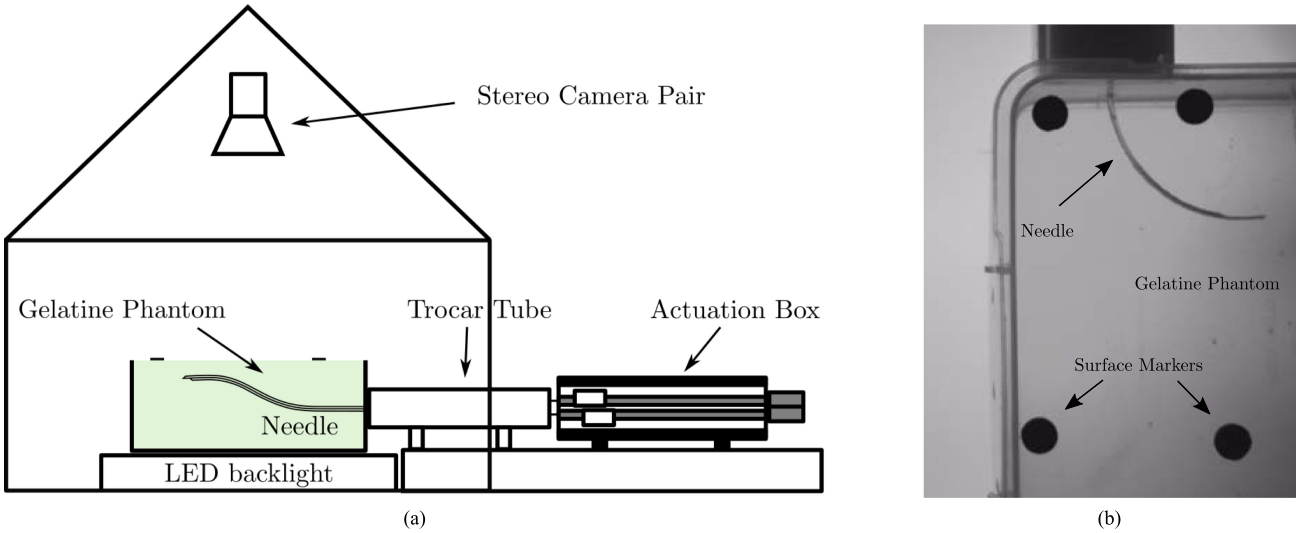

Fig. 10. (a) Diagram of experimental setup. The stereo camera pair tracks the 3-D position of the needle tip within the gelatin phantom. The needle insertion is driven by the actuation system, comprising 4 linear actuators which can independently control each segment. The uninserted needle is supported in the trocar tube, which holds the segments together. (b) Image of needle insertion, as seen from one of the stereo cameras, into the gelatin phantom; the surface markers allow detection of the gelatin plane for refractive index compensation.

with other results, due to the high variability of gelatin mechanical properties across different brands, preparation techniques, and temperatures. However, the achieved curvature is significantly greater than the 0.0083 mm^{-1} reported previously for the flexure-tip needle under similar conditions [33]. We expect this is due to the needle's comparatively low flexural rigidity EI (minimum of 1.62 N mm^2 for a single segment) [2], paired with the relatively large bevel face area.

2) Model Evaluation: The mean experimental curvature vectors, along with a single standard deviation for both magnitude and direction, are plotted for each tip configuration in Fig. 11.

From the plot, we can clearly see the needle is able to steer in any direction. The maximum curvature is achieved in the single segment forward configurations, agreeing with results reported previously by [24], and the model predictions from Section II. This result also agrees with our intuition, as a single segment has the lowest cross-section stiffness and, therefore, is expected to experience the greatest deflection.

The two-segment forward configurations achieved greater curvature than the mixed configurations trialled in this case, a result that may initially be considered counter-intuitive, given that the mixed configurations have a single leading segment. However, the same trend was observed in the FE deflection simulations in Fig. 8 and model predictions in Fig. 7. This indicates that, in going from a two-segment forward to mixed configuration, the reduction in needle-tip stiffness is offset by a comparatively greater reduction in the loading, which is no longer fully applied at the tip. We expect that, for mixed configurations closer to the single segment forward configuration, this tradeoff would be reversed, as is seen in Figs. 7 and 8.

The rotational symmetry of the plotted results reflects the rotational symmetry of the PBN design. The rotational skew effect due to the nonidentity second moment of area tensor is also observed.

3) Best-Fit Model: The experimental curvature vectors from the 16 configurations specified in Table IV were used to conduct a parameter fit, in order to produce a best-fit model.

Of the model parameters presented in Table I, the number of segments $n = 4$, Young's modulus $E = 15$ MPa, and second moment of area tensor

$$\mathbf{I}_1 = \begin{bmatrix} 0.1082 & -0.0229 \\ -0.0229 & 0.2147 \end{bmatrix} \text{mm}^4$$

are known. The remaining model parameters, listed in Table V, were considered in an nonlinear optimization to find the best-fit values that minimize the RMSD between experimental and model predicted curvatures

$$\text{RMSD}(\boldsymbol{\mu}) = \sqrt{\frac{\sum_{q=1}^{N} \|\boldsymbol{\kappa}_{\text{exp},q} - \overline{\boldsymbol{\kappa}}(\boldsymbol{\Theta}_q, \boldsymbol{\mu})\|^2}{N}}$$

where $\boldsymbol{\kappa}_{\text{exp},q}$ is the mean experimental curvature for tip configuration q, which goes from 1 to N. $\overline{\boldsymbol{\kappa}}(\boldsymbol{\Theta}_q, \boldsymbol{\mu})$ is the model predicted curvature for relative offset vector $\boldsymbol{\Theta}_q$ and model parameter vector $\boldsymbol{\mu}$.

The nonlinear optimization was performed with the Mathworks MATLAB `GlobalSearch` function. The force and length parameters were constrained to be greater than zero, and angles were constrained between $\pm 45^\circ$.

The resultant best-fit model parameters are reported in Table V for the full 8-parameter model. The corresponding best-fit model-predicted curvature vectors are plotted in Fig. 11 for the 16 "fitting" configurations identified in Table IV.

To evaluate the predictive capability of the model, the 8 "validation" configurations, not included in the parameter fit, were used. The experimental and model-predicted curvature vectors for the validation configurations, evaluated with the best-fit parameters, are also plotted in Fig. 11. The RMSDs are summarized in Table VI.

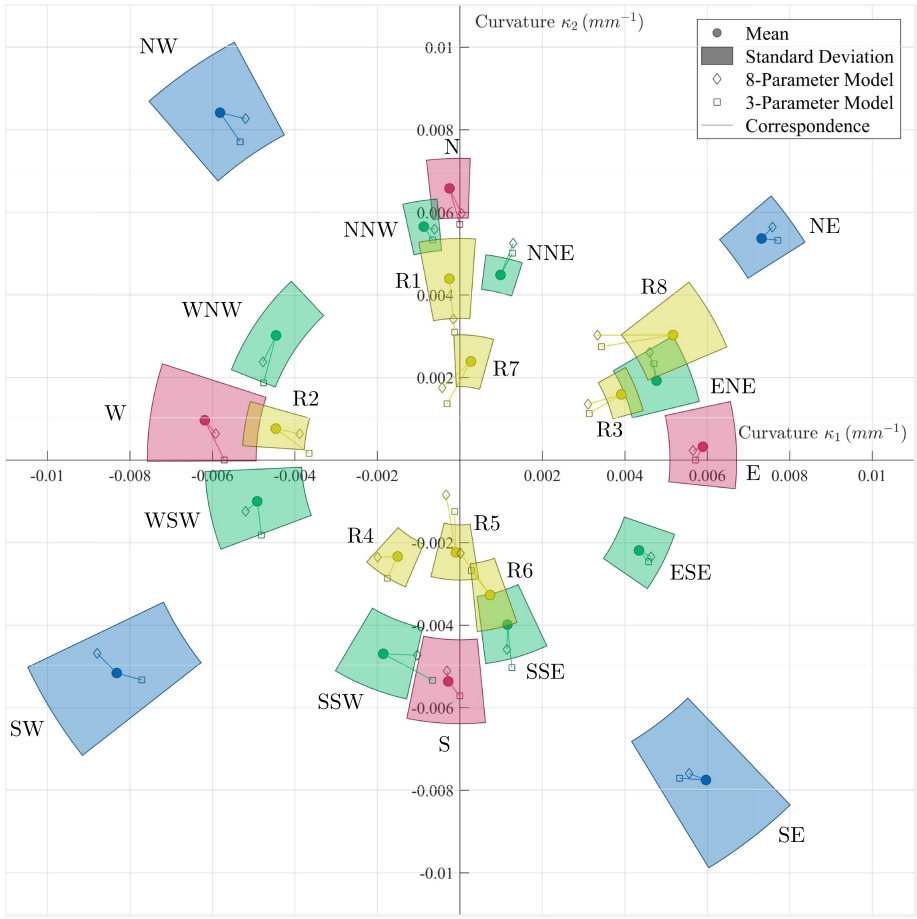

Fig. 11. Curvature vectors are plotted for the tip configurations listed in Table IV. The experimental mean and standard deviation for each configuration's curvature vector are shown. The model-predicted curvatures, evaluated with best-fit parameters, are also plotted for both the 8-parameter and 3-parameter case.

TABLE V
BEST-FIT MODEL PARAMETERS TO EXPERIMENTAL DATA, OBTAINED VIA NONLINEAR OPTIMIZATION

Model parameter	8-parameter best-fit value	3-parameter best-fit value
l	$32.5\,\text{mm}$	$31.0\,\text{mm}$
F_p	$0.00 \times 10^{-3}\,\text{N}$	-
F_c	$3.80 \times 10^{-3}\,\text{N}$	$3.93 \times 10^{-3}\,\text{N}$
l_c	$14.5\,\text{mm}$	$15.8\,\text{mm}$
ϕ_1	$-1.8°$	-
ϕ_2	$8.5°$	-
ϕ_3	$3.2°$	-
ϕ_4	$-2.2°$	-

Values are given for 8-parameter and 3-parameter models.

TABLE VI
RMSD BETWEEN EXPERIMENTAL RESULTS AND MODEL PREDICTIONS

	8-parameter	3-parameter
Fitting	$0.56 \times 10^{-3}\,\text{mm}^{-1}$	$0.77 \times 10^{-3}\,\text{mm}^{-1}$
Validation	$1.12 \times 10^{-3}\,\text{mm}^{-1}$	$1.15 \times 10^{-3}\,\text{mm}^{-1}$
All	$0.79 \times 10^{-3}\,\text{mm}^{-1}$	$0.91 \times 10^{-3}\,\text{mm}^{-1}$

The configurations included in each set (Fitting, Validation) are detailed in Table IV.

For the 8-parameter model, the best-fit value for the deformation force F_p was found to be zero. It should be noted this does not necessarily indicate that the real deformation contribution is negligible. If we consider the form of the assumed loading, as defined in (8), it is greatly simplified. Therefore, differentiating between constant and exponential terms does not directly correspond to separating the deformation and cutting contributions.

Noting that the force angular deviations Φ_i are also small, we consider a parameter reduction. The 3-parameter model considers fitting with only l, F_c, and l_c; all other parameters in Table V are set to zero. Reducing the number of parameters, simplifies the model (and reduces potential sloppiness [21]) so that fewer experimental trials are required for fitting, at the expense of model accuracy. A subsequent optimization was performed for the 3-parameter model, and returned the best-fit values listed in Table I. The RMSD values are also reported in Table VI.

For the model-fitting configurations, and particularly the single and two forward configurations, the 8-parameter model was able to provide a good fit to the experimental data, with RMSD $= 0.56 \times 10^{-3}\ \text{mm}^{-1}$. The increase to RMSD $= 0.77 \times 10^{-3}\ \text{mm}^{-1}$ for the 3-parameter model is modest. For both 8-parameter and 3-parameter models, the unique steering characteristics of the PBN are captured, specifically the relative

curvature magnitudes between different tip configurations and the variation in steering direction, including the clockwise skew due to the nonidentity second moment of area tensor.

The predictive ability of the model is evaluated by comparing the experimental and model-predicted curvature vectors for the validation configurations. The RMSD for the 8-parameter model of 1.12×10^{-3} mm^{-1} is greater than that for the model-fitting configurations, as is to be expected, but all model-predictions fall within two standard deviations of the experimental results. The curvature magnitude is generally underestimated, which could highlight a deficiency in the model requiring further investigation. It is also possible that this error is experimental, given that this latter set of experiments were completed some days after the original set used for model fitting.

Indeed, significant effort was made to mitigate sources of error during the experiments, albeit with such a complex system, identification, and elimination of errors presents a significant challenge. Notable potential sources of discrepancy between experimental and model-predicted results are as follows.

1) Validity of model assumptions, for example the highly simplified point force loading, exponential cutting force, small deflection model, neglected shear strain, and constant segment cross-section.
   a) Small deflection models are generally considered valid for $\left(\frac{dw}{dz}\right)^2 \ll 1$. For the maximum curvature of 0.01 mm^{-1} (model-fitting experiments) and model-fit tip length of 32.5 mm, the maximum $(\frac{dw}{dz})^2 = \tan(0.325)^2 = 0.11$. This is acceptable for the desired model accuracy given the magnitude of other error sources. However, it should be noted that this error term increases in magnitude with higher curvature. In particularly high curvature cases a more complex large-deflection model may be more appropriate.
   b) In order for shear strain effects to be negligible, such that Timoshenko beam theory (commonly used for nonslender beams) is equivalent (for the static case) to Euler–Bernoulli theory, $\frac{EI}{\kappa_t l^2 AG} \ll 1$ should be satisfied. Variables and respective values for our case are: Young's modulus $E = 15$ MPa; Second moment of area $I = 0.2147$ mm^4; Timoshenko shear coefficient $\kappa_t = \frac{5}{6}$; Beam length $l = 32.5$ mm; Cross-sectional area $A = 1.1$ mm^2; Shear modulus $G = 5.64$ MPa. Evaluating yields $\frac{EI}{\kappa_t l^2 AG} = 0.824 \times 10^{-3}$ which confirms that shear strain effects are small in this case.
2) Reliability of manufactured segment tip shape, which may affect the consistency of the forces generated.
3) Experimental errors in needle setup, where the segments must be aligned via sight. Assumed to be of magnitude 0.50 mm.
4) Difference in proximal and distal offsets: see Section V-C for detail. The maximum relative error between the opposing segments is calculated as 1.37 mm with a trajectory average of 0.69 mm. This is comparable in magnitude to other error sources, e.g., initial offset alignment.
5) Variation in gelatin mechanical properties, which affects the forces acting upon the needle.
6) Plasticity of poly(vinyl chloride), such that the needle exhibits some "memory effect", i.e., the curvature vector of a given insertion may be influenced by the previous insertion.

Given the magnitude of experimental variation, the agreement between model predictions and experimental results is acceptable, providing a vast improvement over the linear model, which is currently employed for control of the PBN. The features identified in the experimental curvature plot match those observed in the model predictions, specifically the relative magnitude of the single and two forward configurations, and the skew in steering direction associated with the PBN segment cross-section's nonidentity second moment of area tensor. We, therefore, believe the presented mechanics-based model captures the key steering characteristics of the PBN and its unique multisegment design.

The experimental trials demonstrate, for the first time, that the relative offset for a PBN can be used to control 3-D steering, to achieve curvature in any direction and with variable magnitude. This is the first known passive needle design to achieve such a degree of steerability without the need for axial rotation. We performed the experiments with a clinically sized, medical grade PBN, confirming the potential of the design to target clinical problems.

V. Open-Loop Steering Simulation

A. Trajectory Evolution

The model presented in Section II predicts the instantaneous curvature of the needle tip trajectory, given the current tip configuration. In Section IV, the tip configuration, and therefore model-predicted curvature, was constant over the trajectory and the model need therefore be evaluated only once per trajectory. To predict the evolution of a trajectory for which the tip configuration varies over time we proceed as follows.

Given a relative offset profile $\boldsymbol{\Theta}(t_n)$, which describes the changing needle tip configuration at discrete times t_n, we wish to find the time evolution of the needle tip trajectory $\mathbf{T}_t(t_n)$ as defined in (1). The presented model of Section II is used to evaluate (6) and return the predicted curvature profile $\boldsymbol{\kappa}_P(t_n)$. These curvatures, along with the desired insertion velocity v form the body-frame twist $\boldsymbol{\xi}_P^b(t_n)$ in (4).

The adjoint matrix converts the body-frame twist $\boldsymbol{\xi}_P^b(t_n)$ into the spatial-frame twist $\boldsymbol{\xi}_P^s(t_n)$

$$\boldsymbol{\xi}_P^s(t_n) = \mathbf{Ad}_{6\times 6}(t_n)\boldsymbol{\xi}_P^b(t_n)$$

where

$$\mathbf{Ad}_{6\times 6}(t_n) = \begin{bmatrix} \mathbf{R}_t(t_n) & 0_{3\times 3} \\ \hat{\mathbf{p}}_t(t_n)\mathbf{R}_t(t_n) & \mathbf{R}_t(t_n) \end{bmatrix}$$

and $\hat{\mathbf{p}}_t(t_n)$ is the skew-symmetric matrix formed from $\mathbf{p}_t(t_n)$.

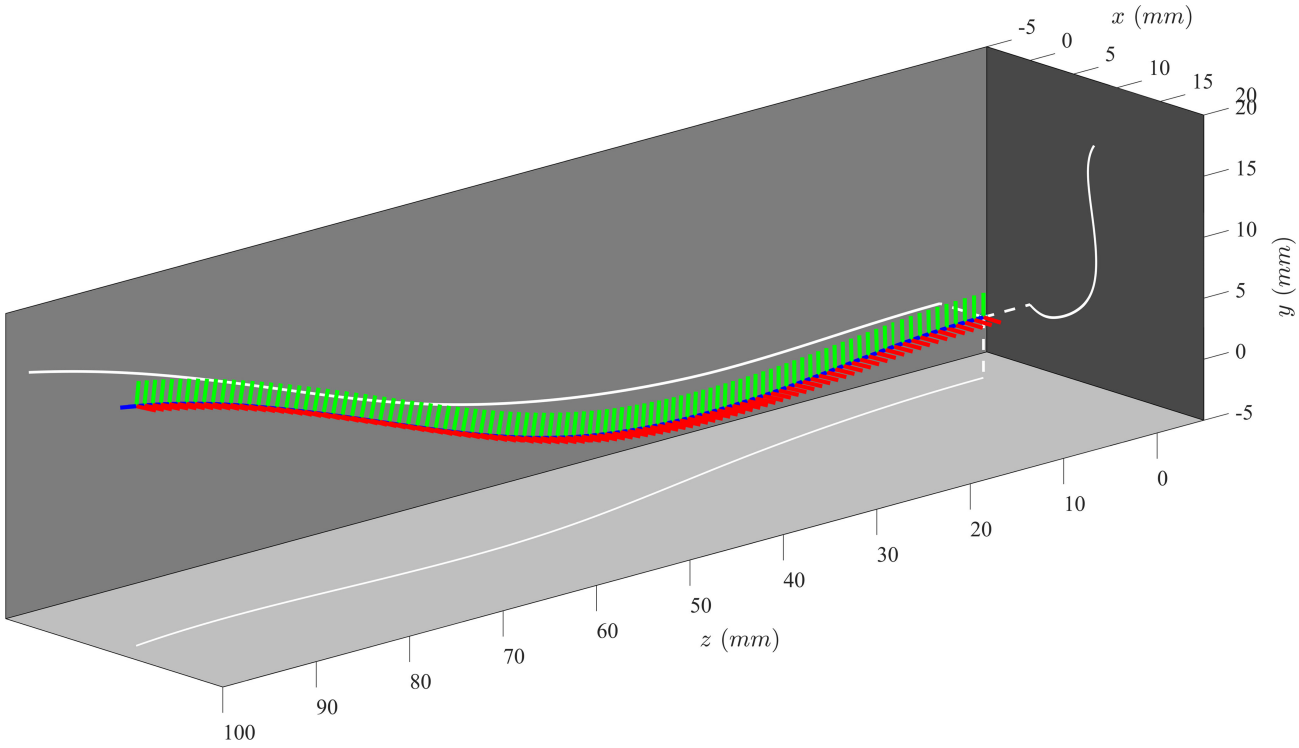

Fig. 12. Plot showing model-predicted 3-D needle trajectory for the open-loop relative offset profile in Section V-B. The coordinate system is shown moving along the trajectory with path projections shown in white.

The spatial-frame twist matrix $\hat{\boldsymbol{\xi}}^s_P(t_n)$, which takes the form of (2), satisfies the following equation:

$$\frac{d\mathbf{T}_t(t_n)}{dt} = \hat{\boldsymbol{\xi}}^s_P(t_n)\mathbf{T}_t(t_n)$$

and therefore the trajectory evolution can be evaluated via the exponential map

$$\mathbf{T}_t(t_{n+1}) = e^{\hat{\boldsymbol{\xi}}^s_P(t_n)dt}\mathbf{T}_t(t_n)$$

where $dt = t_{n+1} - t_n$. Conventionally we choose $\mathbf{T}_t(0) = \mathbf{I}_{4\times4}$, the identity matrix, which locates the origin at the start of the needle trajectory.

B. Three-Dimensional Steering Simulation

We now demonstrate the 3-D trajectory evolution for a specified relative offset profile $\boldsymbol{\Theta}(t_n)$, with $t_n = 0$ to 100 s:

$$\boldsymbol{\Theta}(t_n) = \left[20\cos\left(\frac{2\pi t_n}{100}\right), 20\sin\left(\frac{2\pi t_n}{100}\right), -20\cos\left(\frac{2\pi t_n}{100}\right)\right] \text{mm}$$

The resulting curvature profile $\boldsymbol{\kappa}_P(t_n)$, evaluated with the 8-parameter model, is shown in Fig. 13. The simulated needle trajectory, for insertion speed $v = 1$ mm s^{-1}, is shown in Fig. 12.

It is important to highlight that the model validation of Section IV was only performed for trajectories with constant tip configuration, not the more complex trajectories demonstrated above.

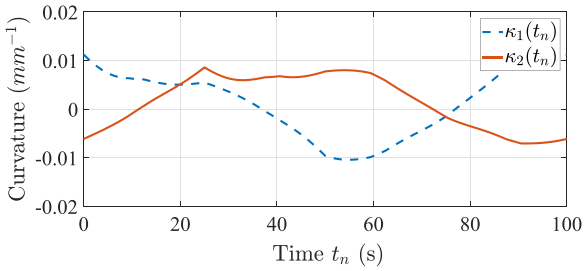

Fig. 13. Plot showing the resulting curvature profile $\boldsymbol{\kappa}_P(t_n)$ for the open-loop relative offset profile in Section V-B.

C. Offset Compensation

The linear actuators control the segment offsets at the proximal end of the needle. Due to the separation between segment neutral axes, there is a path-dependent discrepancy between proximal and distal offsets. Here, we quantify this effect and present an equation to calculate the open-loop compensation required at the proximal end to achieve the desired distal offsets. Note that as a follow on from Assumption 2 in Section II-E, axial compression of segments is not considered as axial stiffness is assumed to be large with respect to axial loads.

The needle's trajectory is described by the motion of the needle tip. Under the established assumption of follow-the-leader motion, the center of the needle's cross-section (origin of the

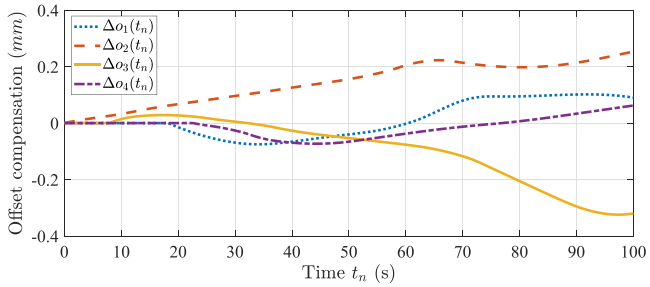

Fig. 14. Plot showing the required offset compensation $\Delta o_i(t_n)$ at the proximal end of the needle for the open-loop relative offset profile in Section V-B. This compensation is calculated according to (19) and ensures that the relative offset at the distal end is as desired, accounting for the path-dependent discrepancy described above.

x_η, y_η axis of Fig. 4) follows this tip trajectory. This trajectory is a development of the twist $\boldsymbol{\xi}_P$ described in (4), with $\boldsymbol{\kappa}_P(s)$ along the path from $s = 0$ to l_{tip}, the insertion length of the tip segment.

Segment i's neutral axis has separation $\boldsymbol{d}_i$ from the needle's center, as shown in Fig. 4. If it is inserted a length l_i, with a straight path assumed prior to $s = 0$, then simple differential geometry yields the expression for its path length discrepancy with respect to the needle center line, Δo_i

$$\Delta o_i = -\int_{s=0}^{l_i} \mathbf{d}_i \cdot \boldsymbol{\kappa}_P(s) ds. \tag{19}$$

Therefore without compensation, the error at the distal end for each segment is $-\Delta o_i$. To achieve desired distal offsets o_i, the required proximal offsets are $o_i' = o_i + \Delta o_i$.

Given the $\mathbf{d}_i$ for the needle, calculated in Dassault Systèmes SolidWorks:

$$\mathbf{d}_1 = \begin{bmatrix} -0.43 \\ 0.61 \end{bmatrix} \text{mm}, \mathbf{d}_2 = \begin{bmatrix} 0.61 \\ 0.43 \end{bmatrix} \text{mm}$$

$$\mathbf{d}_3 = \begin{bmatrix} 0.43 \\ -0.61 \end{bmatrix} \text{mm}, \mathbf{d}_4 = \begin{bmatrix} -0.61 \\ -0.43 \end{bmatrix} \text{mm}.$$

The required compensation for the trajectory presented in Section V-B, calculated via (19), is shown in Fig. 14. By subtracting the calculated offset compensation from the offset profile of Section V-B we can simulate the equivalent uncompensated trajectory (not shown). The Cartesian tip discrepancy between the end of the compensated and noncompensated trajectory is 0.127 mm.

VI. Conclusion and Future Work

Steerable needles have the potential to greatly improve clinical access. To achieve accurate targeting it is crucial that their steering behavior is understood. To this end, we have presented a model for the steering of programmable bevel-tip needles. The model sheds light on the steering mechanism, particularly the importance of the needle's geometry and multisegment design. FE simulations and experiments showed good agreement with model predictions, which captured the unique steering characteristics, due to the multisegment design. The RMSD between the experimental and model predicted curvatures was RMSD $= 1.12 \times 10^{-3}$ mm^{-1}.

In evaluating the model, we also introduced the first clinically-sized, medical-grade PBN, which has been manufactured commercially via extrusion. The 4-segment design includes a functional working channel in each segment, which could be clinically exploited for applications such as drug delivery, optical coherence tomography, laser ablation or cyst evacuation. We showed, through an extensive set of fixed-offset experimental insertions, that the manufactured PBN is capable of steering in any desired direction with variable curvature, without the need for axial rotation.

In future work, we plan to develop a needle simulation platform based on the steering model presented. This will allow further study into possible user-input mappings, control strategies (including human-in-the-loop), and surgical training methods.

The 3-parameter model identified the parameters l, F_c, and l_c, which characterize the tool-tissue interaction, and therefore determine the PBN's steering behavior. We expect these to be a function of the tissue properties: establishing this relationship would allow prediction of the steering ability in different biological tissues. In addition, we plan to carry out a series of *in vivo* trials to evaluate the performance of the model under clinical conditions (e.g., tissue heterogeneity, viscoelasticity, porosity).

We are already working on a demonstration of the needle's ability to describe more complex trajectories with variable curvature magnitude and direction. Future sensorization of individual segments via embedded fiber Bragg grating sensors will allow accurate control of the distal offset and fault detection in the unlikely case of segment separation.

This will be complemented by refinement to the design, informed by the model parameter study, to improve needle steerability and add functionality, e.g., shape-sensing, drug delivery, *in situ* diagnostics.

References

[1] N. Abolhassani, R. Patel, and M. Moallem, "Needle insertion into soft tissue: A survey," *Med. Eng. Phys.*, vol. 29, no. 4, pp. 413–431, 2007.

[2] N. J. Van De Berg, D. J. Van Gerwen, J. Dankelman, and J. J. Van Den Dobbelsteen, "Design choices in needle steering - a review," *IEEE/ASME Trans. Mechatronics*, vol. 20, no. 5, pp. 2172–2183, 2015.

[3] S. P. DiMaio and S. E. Salcudean, "Needle steering and model-based trajectory planning," *Med. Image Comput. Comput.-Assisted Interventions Conf.*, 2003, vol. 2878, pp. 33–40.

[4] J. A. Engh, D. S. Minhas, D. Kondziolka, and C. N. Riviere, "Percutaneous intracerebral navigation by duty-cycled spinning of flexible bevel-tipped needles," *Neurosurgery*, vol. 67, no. 4, pp. 1117–1122, 2010.

[5] V. Kallem and N. Cowan, "Image guidance of flexible tip-steerable needles," *IEEE Trans. Robot.*, vol. 25, no. 1, pp. 191–196, Feb. 2009.

[6] K. B. Reed, A. M. Okamura, and N. J. Cowan, "Modeling and control of needles with torsional friction," *IEEE Trans. Biomed. Eng.*, vol. 56, no. 12, pp. 2905–2916, Dec. 2009.

[7] R. J. Webster, N. J. Cowan, G. S. Chirikjian, and A. M. Okamura, "Nonholonomic modelling of needle steering," *Int. J. Robot. Res.*, vol. 25, no. 5/6, pp. 509–526, 2006.

[8] S. Okazawa, R. Ebrahimi, J. Chuang, S. E. Salcudean, and R. Rohling, "Hand-held steerable needle device," *IEEE/ASME Trans. Mechatronics*, vol. 10, no. 3, pp. 285–296, Jun. 2005.

[9] P. Sears and P. Dupont, "A steerable needle technology using curved concentric tubes," in *Proc. IEEE Int. Conf. Intell. Robots Syst.*, 2006, pp. 2850–2856.

[10] R. J. Webster, A. M. Okamura, and N. J. Cowan, "Toward active cannulas: Miniature snake-like surgical robots," *Proc. IEEE Int. Conf. Intell. Robots Syst.*, 2006, pp. 2857–2863.
[11] L. Frasson, S. Y. Ko, A. Turner, T. Parittotokkaporn, J. F. Vincent, and F. Rodriguez y Baena, "STING: A soft-tissue intervention and neurosurgical guide to access deep brain lesions through curved trajectories," *Proc. Institution Mech. Eng., H, J. Eng. Med.*, vol. 224, no. 6, pp. 775–788, 2010.
[12] M. Scali, D. Kreeft, P. Breedveld, and D. Dodou, "Design and evaluation of a wasp-inspired steerable needle," in *Proc. SPIE. Conf. Bioinspiration, Biomimetics, Bioreplication*, vol. 10162, 2017, Art. no. 1016207.
[13] P. Qi, H. Liu, L. Seneviratne, and K. Althoefer, "Towards kinematic modeling of a multi-DOF tendon driven robotic catheter," *Proc. Int. Conf. IEEE Eng. Med. Biol. Soc.*, 2014, pp. 3009–3012.
[14] R. J. Roesthuis, N. J. Van De Berg, J. J. Van Den Dobbelsteen, and S. Misra, "Modeling and steering of a novel actuated-tip needle through a soft-tissue simulant using Fiber Bragg Grating sensors," in *Proc. IEEE Int. Conf. Robot. Automat.* 2015, pp. 2283–2289.
[15] S. C. Ryu *et al.*, "Design of an optically controlled MR-compatible active needle," *IEEE Trans. Robot.*, vol. 31, no. 1, pp. 1–11, Feb. 2015.
[16] M. Oldfield, D. Dini, G. Giordano, and F. Rodriguez y Baena, "Detailed finite element modelling of deep needle insertions into a soft tissue phantom using a cohesive approach," *Comput. Methods Biomechanics Biomedical Eng.*, vol. 16, no. 5, pp. 530–543, 2013.
[17] R. Alterovitz, K. Goldberg, and A. M. Okamura, "Planning for steerable bevel-tip needle insertion through 2-D soft tissue with obstacles," in *Proc. IEEE Int. Conf. Robot. Automat.*, 2005, pp. 1640–1645.
[18] S. P. DiMaio and S. E. Salcudean, "Interactive simulation of needle insertion models," *IEEE Trans. Biomed. Eng.*, vol. 52, no. 7, pp. 1167–1179, Jul. 2005.
[19] M. Khadem, C. Rossa, N. Usmani, R. S. Sloboda, and M. Tavakoli, "A two-body rigid/flexible model of needle steering dynamics in soft tissue," *IEEE/ASME Trans. Mechatronics*, vol. 21, no. 5, pp. 2352–2364, Oct. 2016.
[20] D. Glozman and M. Shoham, "Flexible needle steering and optimal trajectory planning for percutaneous therapies," in *Proc. Int. Conf. Med. Image Comput. Comput.-Assisted Intervention*, 2004, pp. 137–144.
[21] M. K. Transtrum, B. B. Machta, K. S. Brown, B. C. Daniels, C. R. Myers, and J. P. Sethna, "Perspective: Sloppiness and emergent theories in physics, biology, and beyond," *J. Chem. Phys.*, vol. 143, no. 1, 2015, Art. no. 010901.
[22] S. Y. Ko, L. Frasson, and F. Rodriguez y Baena, "Closed-loop planar motion control of a steerable probe with a programmable bevel inspired by nature," *IEEE Trans. Robot.*, vol. 27, no. 5, pp. 970–983, Oct. 2011.
[23] S. Y. Ko, B. L. Davies, and F. Rodriguez y Baena, "Two-dimensional needle steering with a "programmable bevel" inspired by nature: Modeling preliminaries," in *Proc. Int. Conf. Intell. Robots Syst.*, 2010, pp. 2319–2324.
[24] C. Burrows, R. Secoli, and F. Rodriguez y Baena, "Experimental characterisation of a biologically inspired 3D steering needle," in *Proc. Int. Conf. Control, Automat. Syst.*, 2013, pp. 1252–1257.
[25] R. Secoli and F. Rodriguez y Baena, "Adaptive path-following control for bio-inspired steerable needles," in *Proc. IEEE Int. Conf. Biomed. Robot. Biomechatronics*, 2016, pp. 87–93.
[26] R. Secoli and F. Rodriguez y Baena, "Experimental validation of curvature tracking with a programmable bevel-tip steerable needle," in *Proc. IEEE Int. Symp. Med. Robot*., Mar. 2018, pp. 1–6.
[27] J. M. Selig, *Geometric Fundamentals of Robotics*, (ser. Monographs in Computer Science). New York, NY, USA: Springer, 2005.
[28] J. Selig, "Characterisation of frenetserret and bishop motions with applications to needle steering," *Robotica*, vol. 31, no. 06, pp. 981–992, 2013.
[29] R. L. Bishop, "There is more than one way to frame a curve," *Amer. Math. Monthly*, vol. 82, no. 3, pp. 246–251, 1975.
[30] A. M. Okamura, C. Simone, and M. D. O'Leary, "Force modeling for needle insertion into soft tissue," *IEEE Trans. Biomed. Eng.*, vol. 51, no. 10, pp. 1707–1716, Oct. 2004.
[31] A. Leibinger *et al.*, "Soft tissue phantoms for realistic needle insertion: A comparative study," *Ann. Biomed. Eng.*, vol. 44, no. 8, pp. 2442–2452, 2016.
[32] T. Adebar, J. Greer, P. Laeseke, G. Hwang, and A. Okamura, "Towards robotic needle steering for percutaneous radio frequency ablation in the liver: Procedure-specific workspace analysis," in *Proc Hamlyn Symp. Med. Robot.* 2015, pp. 67–68.
[33] P. J. Swaney, J. Burgner, H. B. Gilbert, and R. J. Webster, "A flexure-based steerable needle: High curvature with reduced tissue damage," *IEEE Trans. Biomed. Eng.*, vol. 60, no. 4, pp. 906–909, Apr. 2013.
[34] G. Franceschini, "The mechanics of human brain tissue," *Modelling, Preservation and Control of Materials and Structures. University of Trento, Trento, Italy,* 2006.
[35] M. A. Poca, F. Martnez-Ricarte, J. Sahuquillo, R. Lastra, R. Torn, and M. S. Armengol, "Intracranial pressure monitoring with the neurodur-p epidural sensor: A prospective study in patients with adult hydrocephalus or idiopathic intracranial hypertension," *J. Neurosurgery*, vol. 108, no. 5, pp. 934–942, 2008.
[36] A. Al-Sharadqah and N. Chernov, "Error analysis for circle fitting algorithms," *Electron. J. Statist.*, vol. 3, pp. 886–911, 2009.

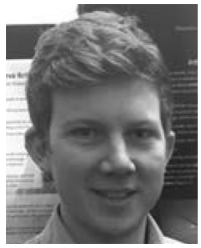

Thomas Watts (S'17) received the M.Eng. degree in mechanical engineering from the University of Cambridge, Cambridge, U.K., in 2014, for which he spent a year enrolled at the Massachusetts Institute of Technology, MA, USA. He is currently pursuing the Ph.D. degree at the Mechatronics in Medicine Laboratory, Imperial College London, London, U.K.

His current research interests include design, modeling and control of surgical robots.

Riccardo Secoli received the M.Sc. degree in computer engineering in 2006 and the Ph.D. degree in industrial engineering (curriculum on Mechatronics and Industrial System) from University of Padova, Padua, Italy, in 2010.

From 2009 to 2011, he was a Postdoctoral Fellow with the BioRobotics Laboratory, University of California Irvine, USA. He is currently a Research Associate with the Mechatronics in Medicine Laboratory, Imperial College London, U.K. His research interests include surgical and rehabilitation robotics design and control.

Ferdinando Rodriguez y Baena (M'09) received the M.Eng. (First-Class Hons.) degree in mechatronics and manufacturing systems engineering from Kings College London, London, U.K., in 2000, and the Ph.D. degree in medical robotics from the Department of Mechanical Engineering, Imperial College London, London, U.K., in 2004.

He is currently a Professor with the Department of Mechanical Engineering, Imperial College London, where he leads the Mechatronics in Medicine Laboratory. His current research interests include the application of mechatronic systems to medicine, in the specific areas of clinical training, diagnostics, and surgical intervention.